

A Progress Report on Laser Resonance Chromatography

Elisa Romero Romero ^{1,2,3,*} , Michael Block ^{1,2,3} , Biswajit Jana ^{1,2,3} , Eunkang Kim ^{1,2,3},
Steven Nothhelfer ^{1,2,3} , Sebastian Raeder ^{2,3} , Harry Ramanantoanina ^{1,2,3}, Elisabeth Rickert ^{1,2,3},
Jonas Schneider ¹, Philipp Sikora ¹ and Mustapha Laatiaoui ^{1,2,3} 

¹ Department Chemie—Standort TRIGA, Johannes Gutenberg-Universität Mainz, 55099 Mainz, Germany

² Helmholtz-Institut Mainz, 55099 Mainz, Germany

³ GSI Helmholtzzentrum für Schwerionenforschung, 64291 Darmstadt, Germany

* Correspondence: eromeror@uni-mainz.de

Abstract: Research on superheavy elements enables probing the limits of nuclear existence and provides a fertile ground to advance our understanding of the atom's structure. However, experimental access to these atomic species is very challenging and often requires the development of new technologies and experimental techniques optimized for the study of a single atomic species. The Laser Resonance Chromatography (LRC) technique was recently conceived to enable atomic structure investigations in the region of the superheavy elements. Here, we give an update on the experimental progress and simulation results.

Keywords: laser spectroscopy; superheavy elements; laser resonance chromatography



Citation: Romero Romero, E.; Block, M.; Jana, B.; Kim, E.; Nothhelfer, S.; Raeder, S.; Ramanantoanina, H.; Rickert, E.; Schneider, J.; Sikora, P.; et al. A Progress Report on Laser Resonance Chromatography. *Atoms* **2022**, *10*, 87. <https://doi.org/10.3390/atoms10030087>

Academic Editor: Christian Parigger

Received: 2 August 2022

Accepted: 31 August 2022

Published: 6 September 2022

Publisher's Note: MDPI stays neutral with regard to jurisdictional claims in published maps and institutional affiliations.



Copyright: © 2022 by the authors. Licensee MDPI, Basel, Switzerland. This article is an open access article distributed under the terms and conditions of the Creative Commons Attribution (CC BY) license (<https://creativecommons.org/licenses/by/4.0/>).

1. Introduction

In the last two decades, there have been outstanding and exceptional efforts in the discovery and study of the superheavy elements [1]. One of the highlights is the completion of the seventh row in the periodic table with the addition of four new synthetic elements in 2016, including oganesson (Og, element number $Z = 118$), the last and heaviest element to date. The development of new selective and efficient techniques has had an impact on the discovery of these elements and their detailed study. Some of these elements are predicted to not behave chemically like their lighter homologs, with relativistic effects being the dominant cause of this peculiarity [2,3].

The challenges to study them are manifold. Superheavy elements are produced in nuclear fusion-evaporation reactions using powerful accelerators at extremely low rates in the presence of a huge background from primary-beam particles. In addition, they usually exist only for a few seconds after their production, which explains why their basic chemical and atomic properties are often not known [1]. Efficient gas chromatography has been used to elucidate the adsorption enthalpies. The heaviest element studied with this technique is flerovium (Fl, $Z = 114$), with a half-life ranging between one and two seconds [4–6]. A few years ago, experiments using surface-ionization techniques were successfully applied to lawrencium (Lr, $Z = 103$), aiming at establishing the element's ionization potential [7].

Deeper insights into the atomic properties and structure can be gained from optical spectroscopy. At present, in-gas-cell laser resonance ionization spectroscopy [8–10] is the most advanced method for atomic structure studies on the heaviest elements. A recent breakthrough in this research field was achieved with the spectroscopy of nobelium (No, $Z = 102$) [10] using the Radiation-Detected-Resonance-Ionization-Spectroscopy (RADRIS) technique.

Our alternative way of optical spectroscopy, namely, Laser Resonance Chromatography, has already been proposed for optical spectroscopy of lawrencium ions and is explained in detail in Ref. [11]. Briefly, this technique combines resonant laser excitation with electronic-state chromatography [12–15] and is conducted directly on the ion in-situ,

without the need for a neutralization step. Given the fusion products are stopped and extracted from a gas catcher in a +1 charge state, a laser of a proper wavelength optically pumps the ions into a metastable state from the ionic ground state. After this step, the ions are injected into a drift tube filled with diluted helium (He) gas, where they undergo a constant drift under the influence of an external electric field. Different interactions of the ions in the different states with helium result in state-specific ion mobilities, which enable modern electronic-state chromatography, i.e., separating the ions in the ground state from the metastable ions by drift time [13,16]. In other words, the changes in the arrival time distributions caused by laser excitations give the resonance signal. Although only applicable to ions and dependent on the presence of metastable states, the method of electronic state chromatography is well established for many elemental cations of the first-, second- and third-row transition metals [17–22].

To this end, a first-generation drift tube chamber has been designed for LRC applications. This design is different from traditional ion-mobility-experiment applications since suppressing deactivation of metastable states is mandatory and is pursued by reducing the length of the tube and operating at relatively low pressures.

In the next two sections, we give a brief report on the experimental progress of the laser resonance chromatography project by presenting the experimental apparatus including the laser system, the cryogenic drift tube, and the corresponding ion trajectory simulations. Due to the scarcity of data and since scandium (Sc, $Z = 21$) can be deemed as a homolog of lutetium (Lu, $Z = 71$), the later simulations were conducted for singly charged scandium in its ground and metastable states of known ion mobilities. In the last section, we give prospects of LRC experiments on Sc^+ , Lu^+ and its heavier iso-electronic system, Lr^+ . A summary of the important properties of these elements is compiled in Table 1.

Table 1. Relevant electronic states in Sc^+ , Lu^+ , and Lr^+ ions. The experimental ion mobilities are given for a helium temperature of 295 K. Predictions are marked by \star .

Ion	Ground State		State to Be Probed		Metastable State			
	Config.	$\bar{\nu}$ (cm^{-1})	K_0 (cm^2/Vs)	Config.	$\bar{\nu}$ (cm^{-1})	Config.	$\bar{\nu}$ (cm^{-1})	K_0 (cm^2/Vs)
Sc^+ ^a	$3d4s\ a^3D_1$	0	22.5	$3d4p\ z^3D_1^o$	27,917.78	$3d^2\ a^3F_2$	4802.87	18.5
Lu^+ ^b	$6s^2\ ^1S_0$	0	16.8	$6s6p\ ^3P_1^o$	28,503.16	$5d6s\ ^3D_1$	11,796.24	19.5 \star
Lr^+ ^c	$7s^2\ ^1S_0$	0	16.8 \star	$7s7p\ ^3P_1^o$	31,540 \star	$6d7s\ ^3D_1$	20,846 \star	19.4 ^d \star

^a: Refs. [23–25]; ^b: Refs. [26–28]; ^c: Ref. [28–30]; ^d: Ref. [31].

2. Experimental Approach

Laser resonance chromatography couples laser spectroscopy with ion mobility spectrometry. It is based on a population transfer between metastable ionic states in a resonant laser excitation process. A laser excites the ion, e.g., from the ground state to an intermediate level (to be optically probed) in an allowed optical transition. The intermediate level depopulates partly to lower-lying metastable states that do not easily quench to the ground state. In a simplified picture, the ion changes its size during this process, which can then be exploited for purposes of diagnostics. The resonant process is identified by a change in the characteristic arrival-time distributions of the ions on a particle detector after passing a drift tube filled with helium gas at pressures < 10 mbar. Since the mobility is function of the gas temperature and could be distinct for the different states, the operation of the drift tube at cryogenic temperatures usually provides an additional degree of freedom to optimize time resolution and state separation [19,32].

The method is generally applicable for transition-metal ions including Lu^+ and Lr^+ . Promising optical pumping schemes for singly charged rutherfordium, the next-heavier element within the fourth row transition metals, have already been proposed [33]. Compared to many existing spectroscopy techniques, the LRC approach has a number of key advantages, some of which are:

- No neutralization of the thermalized fusion products is required. The ions can be manipulated and guided with high efficiency by electric fields;
- No further ionization of the ions is required. Only one laser is needed for spectroscopy;
- No radiation detection is required as in fluorescence spectroscopy. The sensitivity does not depend on the solid angle coverage of the detectors;
- A mass filter is a useful option at low ion production rates, but is not mandatory to suppress molecular sidebands or even isobars of different electronic configurations, as the drift itself provides the required ion discrimination.

2.1. The LRC Apparatus

The LRC setup is shown in Figure 1. It consists of five different pressure sections (PS) for stopping, extraction, separation, mass selection and detection of the sample ions. The ionized residual nuclei produced during the fusion-evaporation process lose most of their kinetic energy by passing through a metallic window of a few μm thickness before they are thermalized by collisions with the He buffer gas inside of the stopping cell (PS1) at a pressure of about 60 mbar. The thermalized ions are ejected through a convergent–divergent nozzle of 0.6 mm throat diameter towards a radio frequency quadrupole (RFQ) in PS2 that serves to extract and further cool the ions and to guide them towards the buncher in the next pumping section (PS3). The first-generation stopping cell of the SHIPTRAP setup together with its extraction RFQ is used for this purpose [34].

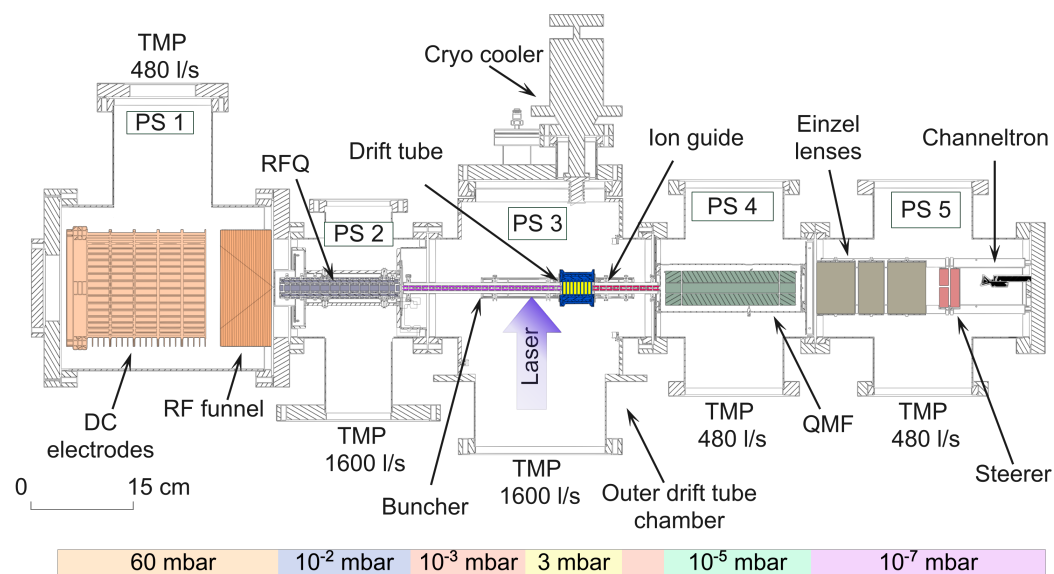


Figure 1. Schematic overview of the LRC apparatus. See text for more information.

The subsequent buncher installation enables a spatial confinement of the ions for laser spectroscopy and a precise referencing of their arrival time distributions. It consists of four stainless steel rods with diameters of 3.5 mm, each divided into 25 segments. The distance between opposite rods is $2r_0 = 3$ mm. PS3 also incorporates a cryogenic drift tube and an ion guide. The drift tube is used for electronic-state chromatography and is explained in more detail in Section 2.3. The ion guide comprises 10 segments of similar geometry as the buncher segments and is used to transport and focus the ions into the quadrupole mass filter (Extrel QMS) in the pumping section PS4, where the ions are selected based on their mass-to-charge ratio. Next, the ions are focused by einzel lenses and a X and Y steerer towards the detection system, which contains a channeltron detector (Dr Sjuets K15) installed in the last pumping section PS5.

(M2, DIN 975/DIN 976 Titanium Grade 2). The drift tube chamber is plated on the outside with a thin copper layer of 50–100 μm thickness to enable better heat conductance and a homogeneous distribution of the temperature over the whole drift tube during cooling and warming phases. It includes a gas inlet and outlet, a connection for a pressure gauge (Pfeiffer Vacuum PKR 360) and several tapered holes to fix heaters (high power resistors TCP100U) and temperature sensors (Lake Shore Germanium-CD). The tube has octagonal flanges at both ends that also serve to attach it to the spokes on the outer chamber.

In its interior, the drift tube chamber incorporates eight stainless steel electrodes of 20 mm inner diameter, 24 mm outer diameter and of a width of 5 mm. Six of the electrodes are enclosed by two identical end caps designed to have an electrode in one side and a diaphragm of 1 mm on the other side, serving either as injection or exit nozzle. The caps also serve as a support for the stainless steel fixation of the buncher and the ion guide; cf. Figure 3. All inner electrodes are electrically connected to each other by seven 1-M Ω resistors in series to build up a resistance of 7.15 M Ω between the end caps. The electrodes are supported via Vitronit ceramic rods of 5 mm diameter and 46.5 mm length and separated by 0.5 mm from each other with Vitronit ceramic cylindrical spacers of 5 mm length and 5 mm inner diameter. All inner electrodes plus the end caps are surrounded by a ceramic cylinder of 40 mm inner diameter, 44 mm outer diameter and length of 46.5 mm to isolate the electrodes from the grounded tube housing.

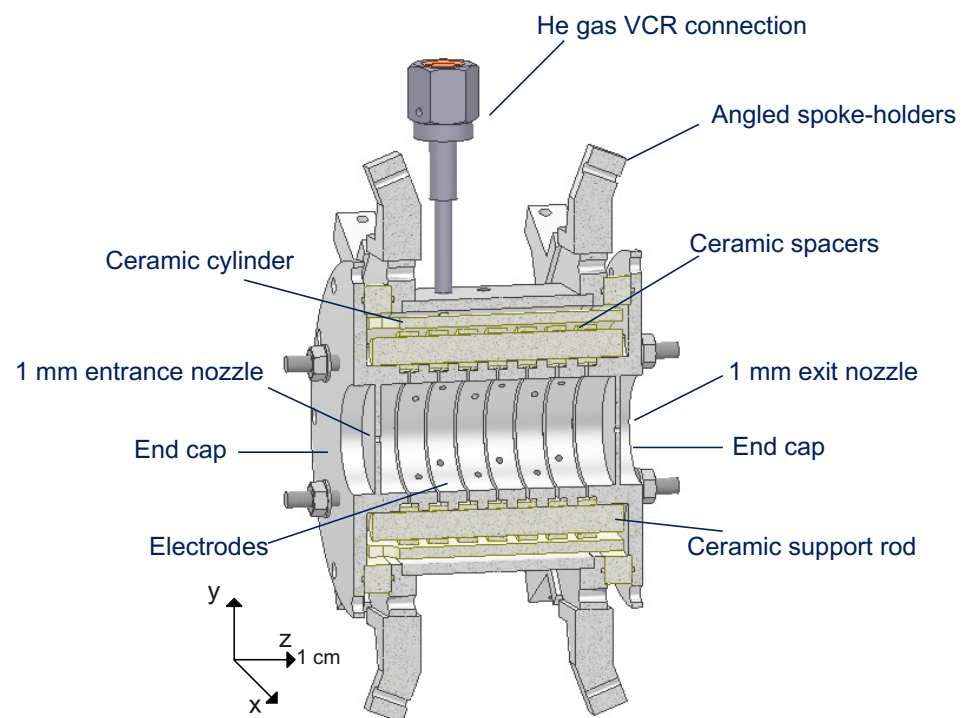


Figure 3. 3D cross-sectional view of the LRC drift tube and its components.

3. Ion Drift Simulations

Simulations were performed for the drift tube using the SIMION software package [35] in order to estimate Sc^+ drift times at a given He pressure and temperature and to extract suitable voltage configurations to be used in future LRC experiments. In the simulations, we considered both Statistical Diffusion (SDS) and Viscous Damping (VD) models [36]. Hard sphere model simulations could not be performed thus far due to the lack of reference data for the collision cross sections.

The reduced mobility for Sc^+ in the ground state and Sc^{+*} in the metastable state for the SDS and VD models were taken from [20]; cf. Table 1. We tested two configurations, one with a roughly constant electric field (unfocused beam) and a second with a gradually increasing electric field (focused beam). Ions were generated at the entrance of the drift

tube and their drift times were recorded when they exited through a 1 mm or 2 mm diameter nozzle to explore the feasibility of enhancing the transmission while keeping time resolution unchanged. The two voltage configurations we used are shown in Table 2. We simulated different voltage values of U_0 in a way that the resulting average ratio of electric-field strength to gas number density, E/n_0 , spanned a range between 1 and 30 Td, with $1 \text{ Td} = 10^{-17} \text{ V} \cdot \text{cm}^2$. For each value of U_0 , 10,000 ions were generated in a 3D Gaussian distribution with a standard deviation of $\sigma_{x,y,z} = 0.2 \text{ mm}$. The ion mobilities were calculated from the reduced mobilities by considering a pressure of 2 mbar of helium gas at a temperature of $T = 297 \text{ K}$. Figure 4a shows ion trajectories projected on the symmetry plane obtained for the two different electric field configurations at an average reduced field of 15 Td. Using the VD model, the electric fields acting on each ion during its drift were recorded for each voltage configuration and allowed us to extract the mean electric field; cf. Figure 4b.

Table 2. Voltage configurations for unfocused (*) and focused beam (**). n is the electrode number. In the case of the unfocused beam, the voltages applied to the different electrodes were scaled by n, whereby values of U_0 between 0.1–10 V were applied in steps of 0.1 V to span a range of E/n_0 between 1–30 Td. For the focused beam, we added different offsets to the unfocused beam configurations as given in the table, where $\delta = 0.75 \text{ V}$ and U_0 was varied between 0.1–2.7 V to span in total an E/n_0 range between 1–30 Td.

Electrode # n	Unfocused beam Voltage (V) *			Focused beam Voltage (V) **		
1			0			0
2			0			0
3			0			0
4			0			δ
5	$n \cdot U_0$	+	0	$n \cdot U_0$	+	3δ
6			0			7δ
7			0			12δ
8			0			24δ

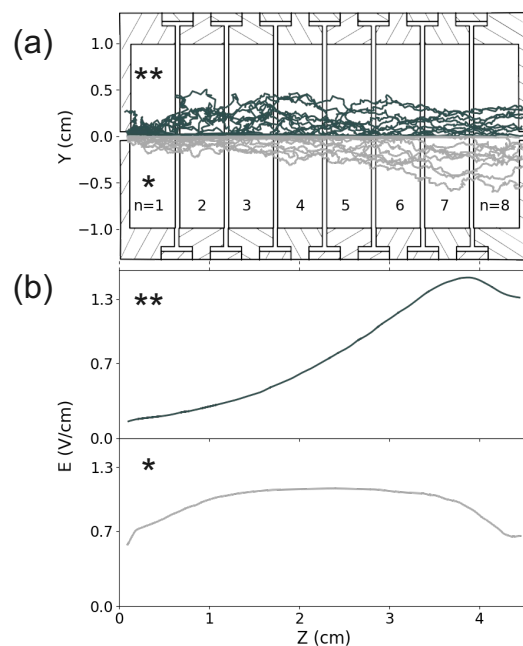


Figure 4. (a) Trajectories for $E/n_0 = 15 \text{ Td}$ for unfocused (*) and focused beams (**). (b) Electric fields along the electrodes for focused (top) and unfocused (bottom) beams.

Results

We made a comparison of the transmission efficiency between focused and unfocused beam configurations and between 1 mm and 2 mm exit nozzles for Sc^+ ions. To this end, we defined this efficiency as the fraction of the number of ions arriving at the exit nozzle within a radius of 0.5 mm (1 mm) from the center axis respective to the initial number of ions for 1 mm (2 mm) nozzle diameters. Figure 5 shows this transmission efficiency for the different states as function of the reduced field. For the unfocused beam using the 1 mm diameter exit nozzle, it grows quickly as the reduced field increases to reach a maximum of 3.7% at an E/n_0 value of about 8.5 Td and decreases with increasing fields to stagnate at about 2%. When using the 2 mm diameter exit nozzle, it grows even quicker as the reduced field increases to reach a maximum of 4.6% at an E/n_0 value of about 7.6 Td and stays stable up to around 20 Td to then increase again. According to the simulations, there is nearly no difference for the unfocused beam in terms of transmission efficiency between the ground and the metastable state for both 1 mm and 2 mm exit diameters below 20 Td. In the case of a focused beam using the 1 mm exit nozzle, the efficiency follows the unfocused beam up to 3 Td, then gradually increases with increasing fields, but stays below that achieved for the unfocused beam till reaching 15 Td. In the case of the 2 mm nozzle, the focused beam and the unfocused beam have similar transmission up to 10 Td. From these values onward for both nozzles, 1 mm and 2 mm, the deviation in the transmission of the two states becomes apparent. A maximum transmission efficiency of 7% for 1 mm and 20% for 2 mm nozzles in the focused beam configuration is achieved for the ground state ions at 30 Td, while the metastable state transmission stagnates at about 5% and 15% for 1 mm and 2 mm, respectively. Since the ions in the ground state exhibit a higher mobility, they can drift faster compared with the ions in the metastable states and thus are less prone to transversal diffusion losses. Theoretically, even higher efficiencies can be expected for these latter scenarios if the reduced field is increased beyond 30 Td, but only at the cost of deactivating states due to gas collisions that would degrade the metastable signal [17,37,38]. In addition, increased electric fields carry the risk of gas discharges with only a few hundred volts for 2 mbar of He gas and lead to shorter drift times due to higher velocity, which can in turn lead to both neutralization and a lower resolving power, respectively.

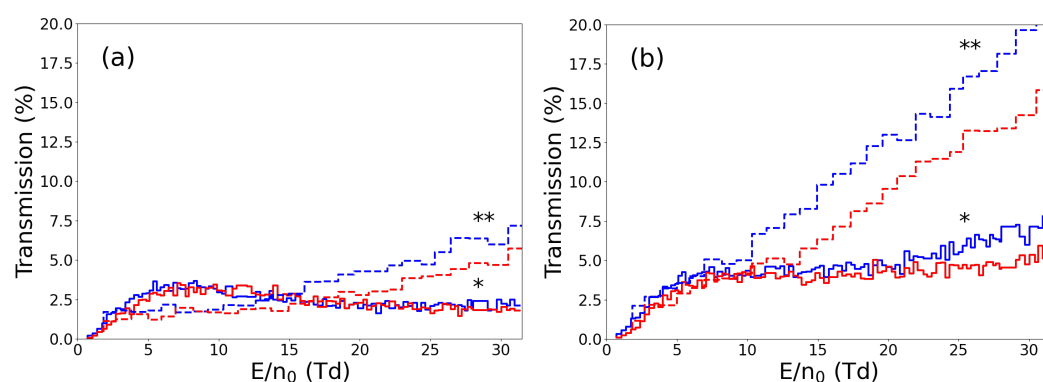


Figure 5. Ion transmission for unfocused (*) and focused (**) beams for both ground (blue) and metastable states (red) and for (a) 1 mm and (b) 2 mm exit diameter nozzles. Dash-line: focused beam; solid line: unfocused beam.

To better understand the behavior of the different electric field configurations in terms of resolution, we analyzed the drift time differences between the ground state and metastable state. Figure 6 shows the drift time for the two Sc^+ states in the different beam configurations in the case of the 1 mm nozzle; similar behavior was observed for the 2 mm exit diameter nozzle. It becomes apparent that, irrespective of the electronic states, the gradual increase of the electric field (corresponding to the beam focusing scenario) cause the ions to drift at small velocities the majority of the time and to lag behind in comparison when

they are exposed to an average but rather homogeneous electric field (unfocused beam). The relative drift time differences exhibit a maximum at reduced field values between 5 Td and 10 Td in both configurations, indicating the best time resolution. However, a deeper insight is obtained by including peak broadening effects in the analysis by comparing the time histograms of the transmitted ions from the simulations. The different ionic states can be disentangled better from each other at larger reduced fields, which means at smaller absolute drift times and thus at the cost of relative drift time differences. If we compare the two different configurations, it becomes clear that, here as well, the unfocused beam provides better working conditions because it provides better time resolution over a larger range of E/n_0 values. In the case of a focused beam, the time peaks can be partly disentangled only at fields higher than ≈ 10 Td. The 2 mm configuration shows a similar trend with respect to the resolution. However, even though the larger nozzle provides higher efficiency, this latter is not so remarkably higher as to trade off the vacuum conditions inside of the PS3 section. We can consider this option for future tests.

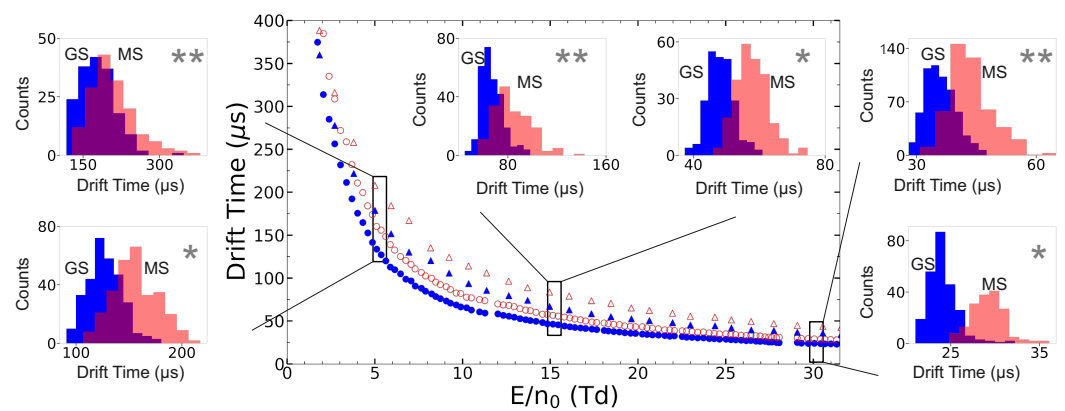


Figure 6. Absolute drift time comparison between ground and metastable states for both focused and unfocused beams. Unfocused beam: ● = ground state; ○ = metastable state. Focused beam: ▲ = ground state; △ = metastable state. Insets: selected histograms for $E/n_0 = 5, 15,$ and 30 Td to demonstrate resolution behavior. * = unfocused beam ; ** = focused beam; blue = ground state; red = metastable state.

4. Current Status and Outlook

In the summer of 2022, the LRC setup is nearly complete and the commissioning phase has already begun with testing of the vacuum and functionality of key components such as the buffer gas stopping cell, the quadrupole mass filter and the laser systems. The cryogenic drift tube together with the miniature ion guide and buncher are being assembled and are ready for integration into the setup. Different ion sources are available, including a laser ablation source and a ^{223}Ra recoil ion source, with the latter being best suited for optimizing and quantifying the transmission efficiency through the whole apparatus.

SIMION simulations were performed for the LRC drift tube using two electric field configurations: unfocused and focused beams; and two geometry configurations: 1 mm and 2 mm exit nozzle diameters. From these simulations, we inferred that a rather homogeneous electric field enables a comparably higher ion transmission while maintaining a good resolution at relatively low E/n_0 values using a 1 mm exit diameter nozzle. In addition, it can be expected that working at lower fields minimizes the risk of gas discharges and deactivation of states. This can therefore also be very beneficial for a successful application of the LRC method. Higher transmission can be achieved when using a 2 mm exit nozzle and eventually focusing the beam into the nozzle.

Our first proof-of-principle experiments will target $^{45}\text{Sc}^+$, cf. Table 1. These offline measurements are currently being prepared and we expect them to last for up to one year. The relative mobility difference between the ground and the metastable state is about 20% at 295 K in He [25], which should be sufficient to enable LRC measurements. The laser

probing occurs inside the buncher, i.e. before the ion drift, via laser resonant excitation of the $z^3D_1^o$ state at $27,917.78\text{ cm}^{-1}$ to optically pump the ion into the metastable state a^3F_2 at 4802.87 cm^{-1} . Since the metastable state is energetically relatively close to the ground state, deactivation of states will likely occur during the ion-atom collisions [39]. If such collisional de-excitations dominate and entirely prevent the chromatography of Sc^+ , we will pursue LRC experiments on $^{175}\text{Lu}^+$, the lighter chemical homologue of Lr^+ . In the Lu^+ experiments, we will probe the $^3P_1^o$ state at $28,503.16\text{ cm}^{-1}$ that feeds the 3D_1 metastable state at $11,796.24\text{ cm}^{-1}$. Since this latter state is energetically high enough above the ground state, level crossings in the corresponding diabatic potential curves become unlikely. Thus, for short drift paths, as in the LRC experiments, we expect deactivation of states to be suppressed in Lu^+ -He collisions, particularly at moderate kinetic energies. Here, one should note that in Ref. [25], the signal of the metastable state could still be observed even for Sc^+ drifting inside a drift tube of about 2 m length. However, since the drift tube of the LRC apparatus is only 45 mm long, the chromatography will require detailed analysis of the arrival-time distributions due to expected moderate time resolution; cf. Figure 6.

Applying the LRC technique to stable Lu ions can give us a better understanding of the trade-off we should make to achieve maximum count rates without losing the chromatography information. Once experimentally optimized for low yields, LRC can then be applied to search for atomic levels in the heavier iso-electronic system $^{255}\text{Lr}^+$ in on-line experiments.

Author Contributions: Conceptualization, M.L.; Setup design, E.R.R and M.L.; Simulations, E.R.R.; Simulations Methodology, E.R.R. and M.L.; Formal analysis, E.R.R.; Funding acquisition, M.L.; Investigation, E.R.R. and M.L.; Project administration, M.L.; Resources, B.J., E.K., H.R., E.R. and J.S.; Software, E.R.R.; Supervision, M.B. and M.L.; Validation, E.R.R, M.B., S.R. and M.L.; Visualization, E.R.R.; Writing—original draft, E.R.R; Writing—review & editing, E.R.R., M.B., M.L., S.N., S.R. and P.S. All authors have read and agreed to the published version of the manuscript.

Funding: This project has received funding from the European Research Council (ERC) under the European Union's Horizon 2020 Research and Innovation Programme (Grant Agreement No. 819957).

Institutional Review Board Statement: Not applicable.

Informed Consent Statement: Not applicable.

Data Availability Statement: Not applicable.

Acknowledgments: We would like to thank the workshops of the Chemistry, Nuclear Chemistry, Physics and Nuclear Physics departments of the JGU Mainz.

Conflicts of Interest: The authors declare no conflict of interest.

Abbreviations

The following abbreviations are used in this manuscript:

LRC	Laser Resonance Chromatography
SHE	Super Heavy Elements
PS	Pressure Section
SDS	Statistical Diffusion Simulation
VD	Viscous Damping

References

1. Giuliani, S.A.; Matheson, Z.; Nazarewicz, W.; Olsen, E.; Reinhard, P.G.; Sadhukhan, J.; Schuettrumpf, B.; Schunck, N.; Schwerdtfeger, P. Colloquium: Superheavy elements: Oganesson and beyond. *Rev. Mod. Phys.* **2019**, *91*, 011001. [[CrossRef](#)]
2. Nazarewicz, W. The limits of nuclear mass and charge. *Nat. Phys.* **2018**, *14*, 537–541. [[CrossRef](#)]
3. Düllmann, C.E. Studying chemical properties of the heaviest elements: One atom at a time. *Nucl. Phys. News* **2017**, *27*, 14–20. [[CrossRef](#)]
4. Yakushev, A.; Gates, J.M.; Türler, A.; Schädel, M.; Düllmann, C.E.; Ackermann, D.; Andersson, L.L.; Block, M.; Bröchle, W.; Dvorak, J.; et al. Superheavy element flerovium (element 114) is a volatile metal. *Inorg. Chem.* **2014**, *53*, 1624–1629. [[CrossRef](#)]

5. Eichler, R.; Aksenov, N.; Albin, Y.V.; Belozerov, A.; Bozhikov, G.; Chepigin, V.; Dmitriev, S.; Dressler, R.; Gäggeler, H.; Gorshkov, V.; et al. Indication for a volatile element 114. *Rca-Radiochim. Acta* **2010**, *98*, 133–139. [[CrossRef](#)]
6. Yakushev, A.; Lens, L.; Düllmann, C.E.; Block, M.; Brand, H.; Calverley, T.; Dasgupta, M.; Di Nitto, A.; Götz, M.; Götz, S.; et al. First study on nihonium (Nh, element 113) chemistry at TASCA. *Front. Chem.* **2021**, *9*, 753738. [[CrossRef](#)]
7. Sato, T.K.; Sato, N.; Asai, M.; Tsukada, K.; Toyoshima, A.; Ooe, K.; Miyashita, S.; Schädel, M.; Kaneya, Y.; Nagame, Y.; et al. First successful ionization of Lr ($Z = 103$) by a surface-ionization technique. *Rev. Sci. Instrum.* **2013**, *84*, 023304. [[CrossRef](#)]
8. Block, M.; Giacoppo, F.; Heßberger, F.P.; Raeder, S. Recent progress in experiments on the heaviest nuclides at SHIP. *Riv. Nuovo C* **2022**, *45*, 279–323. [[CrossRef](#)]
9. Ferrer, R.; Barzakh, A.; Bastin, B.; Beerwerth, R.; Block, M.; Creemers, P.; Grawe, H.; de Groote, R.; Delahaye, P.; Fléchar, X.; et al. Towards high-resolution laser ionization spectroscopy of the heaviest elements in supersonic gas jet expansion. *Nat. Commun.* **2017**, *8*, 14520. [[CrossRef](#)]
10. Laatiaoui, M.; Lauth, W.; Backe, H.; Block, M.; Ackermann, D.; Cheal, B.; Chhetri, P.; Düllmann, C.E.; Van Duppen, P.; Even, J.; et al. Atom-at-a-time laser resonance ionization spectroscopy of nobelium. *Nature* **2016**, *538*, 495–498. [[CrossRef](#)]
11. Laatiaoui, M.; Buchachenko, A.A.; Viehland, L.A. Laser Resonance Chromatography of Superheavy Elements. *Phys. Rev. Lett.* **2020**, *125*, 023002. [[CrossRef](#)]
12. Backe, H.; Lauth, W.; Block, M.; Laatiaoui, M. Prospects for laser spectroscopy, ion chemistry and mobility measurements of superheavy elements in buffer-gas traps. *Nucl. Phys. A* **2015**, *944*, 492–517. [[CrossRef](#)]
13. Laatiaoui, M.; Backe, H.; Habs, D.; Kunz, P.; Lauth, W.; Sewtz, M. Low-field mobilities of rare-earth metals. *Eur. Phys. J. D* **2012**, *66*, 232. [[CrossRef](#)]
14. Baumbach, J. Ion mobility spectrometry in scientific literature and in the International Journal for Ion Mobility Spectrometry (1998–2007). *Int. J. Ion Mobil. Spectrom.* **2008**, *11*, 3–11. [[CrossRef](#)]
15. Mason, E.A.; McDaniel, E.W. *Transport Properties of Ions in Gases*; Wiley Online Library: Hoboken, NJ, USA, 1988; Volume 26.
16. Kemper, P.R.; Bowers, M.T. State-selected mobilities of atomic cobalt ions. *J. Am. Chem. Soc.* **1990**, *112*, 3231. [[CrossRef](#)]
17. Kemper, P.R.; Bowers, M.T. Electronic-state chromatography: Application to first-row transition-metal ions. *J. Phys. Chem.* **1991**, *95*, 5134–5146. [[CrossRef](#)]
18. Iceman, C.; Rue, C.; Moision, R.M.; Chatterjee, B.K.; Armentrout, P.B. Ion mobility studies of electronically excited states of atomic transition metal cations: Development of an ion mobility source for guided ion beam experiments. *J. Am. Soc. Mass Spectrom.* **2007**, *18*, 1196. [[CrossRef](#)]
19. Ibrahim, Y.; Alsharaeh, E.; Mabrouki, R.; Momoh, P.; Xie, E.; El-Shall, M.S. Ion mobility of ground and excited states of laser-generated transition metal cations. *J. Phys. Chem. A* **2008**, *112*, 1112–1124. [[CrossRef](#)]
20. Manard, M.J.; Kemper, P.R. Ion Mobility Mass Spectrometry: The design of a new high-resolution mobility instrument with applications toward electronic-state characterization of first-row transition metal cations. *Int. J. Mass Spectrom.* **2016**, *402*, 1–11. [[CrossRef](#)]
21. Manard, M.J.; Kemper, P.R. Characterizing the electronic states of the second-row transitionmetal cations using high-resolution ion mobility mass spectrometry. *Int. J. Mass Spectrom.* **2016**, *407*, 69–76. [[CrossRef](#)]
22. Manard, M.J.; Kemper, P.R. An experimental investigation into the reduced mobilities of lanthanide cations using high-resolution ion mobility mass spectrometry. *Int. J. Mass Spectrom.* **2017**, *423*, 54–58. [[CrossRef](#)]
23. Lawler, J.E.; Dakin, J.T. Absolute transition probabilities in Sc I and Sc II. *J. Opt. Soc. Am. B* **1989**, *6*, 1457. [[CrossRef](#)]
24. Kramida, A.; Ralchenko, Y.; Reader, J. *NIST Atomic Spectra Database (Ver. 5.7.1)*; National Institute of Standards and Technology: Gaithersburg, MD, USA, 2020. [[CrossRef](#)]
25. Manard, M.J.; Kemper, P.R. Reduced mobilities of lanthanide cations measured using high-resolution ion mobility mass spectrometry with comparisons between experiment and theory. *Int. J. Mass Spectrom.* **2017**, *412*, 14. [[CrossRef](#)]
26. Quinet, P.; Palmeri, P.; Biémont, E.; McCurdy, M.M.; Rieger, G.; Pinnington, E.H.; Wickliffe, M.E.; Lawler, J.E. Experimental and theoretical radiative lifetimes, branching fractions and oscillator strengths in Lu II. *Mon. Not. Royal Astron. Soc.* **1999**, *307*, 934. [[CrossRef](#)]
27. Arifin. Lutetium Ion Spectroscopy. Bachelor's Thesis, Department of Physics, National University of Singapore, Singapore, 2014.
28. Visentin, G.; Laatiaoui, M.; Viehland, L.A.; Buchachenko, A.A. Mobility of the Singly-Charged Lanthanide and Actinide Cations: Trends and Perspectives. *Front. Chem.* **2020**, *8*, 438. [[CrossRef](#)] [[PubMed](#)]
29. Kahl, E.V.; Berengut, J.C.; Laatiaoui, M.; Eliav, E.; Borschevsky, A. High-precision ab initio calculations of the spectrum of Lr⁺. *Phys. Rev. A* **2019**, *100*, 062505. [[CrossRef](#)]
30. Ramanantoanina, H.; Borschevsky, A.; Block, M.; Laatiaoui, M. Electronic Structure of Lr⁺ ($Z = 103$) from Ab Initio Calculations. *Atoms* **2022**, *10*, 48. [[CrossRef](#)]
31. Ramanantoanina, H.; Borschevsky, A.; Block, M.; Laatiaoui, M. State specific mobility of Lr⁺ ion in He. *Phys. Rev. A* **2022**, *Manuscript in preparation*.
32. Buchachenko, A.A.; Visentin, G.; Viehland, L.A. Gaseous transport properties of the ground and excited Cr, Co and Ni cations in He: Ab initio study of electronic state chromatography. *J. Chem. Phys.* **2022**, *in press*. [[CrossRef](#)]
33. Ramanantoanina, H.; Borschevsky, A.; Block, M.; Laatiaoui, M. Electronic structure of Rf⁺ ($Z = 104$) from ab initio calculations. *Phys. Rev. A* **2021**, *104*, 022813. [[CrossRef](#)]

34. Neumayr, J.B.; Beck, L.; Habs, D.; Heinz, S.; Szerypo, J.; Thierolf, P.G.; Varentsov, V.; Voit, F.; Ackermann, D.; Beck, D.; et al. The ion-catcher device for SHIPTRAP. *Nucl. Instrum. Methods Phys. Res. B* **2006**, *244*, 489. [[CrossRef](#)]
35. Scientific-Instrument-Services. SIMION 8.0. Available online: <https://simion.com/> (accessed on 9 July 2022).
36. Appelhans, A.D.; Dahl, D.A. SIMION ion optics simulations at atmospheric pressure. *Int. J. Mass Spectrom.* **2005**, *244*, 1–14. [[CrossRef](#)]
37. Wilkins, C.L.; Trimpin, S. *Ion Mobility Spectrometry-Mass Spectrometry: Theory and Applications*; CRC Press: Boca Raton, FL, USA, 2010.
38. Loh, S.; Fisher, E.; Lian, L.; Schulz, R.; Armentrout, P. State-specific reactions of Fe+ (6D, 4F) with O2 and c-C2H4O: D° 0 (Fe+-O) and effects of collisional relaxation. *J. Phys. Chem.* **1989**, *93*, 3159–3167. [[CrossRef](#)]
39. Chhetri, P.; Ackermann, D.; Backe, H.; Block, M.; Cheal, B.; Düllmann, C.E.; Even, J.; Ferrer, R.; Giacoppo, F.; Götz, S.; et al. Impact of buffer gas quenching on the $^1S_0 \rightarrow ^1P_1$ ground-state atomic transition in nobelium. *Eur. Phys. J. D* **2017**, *71*, 195. [[CrossRef](#)]